Supporting Information

Synergy of Polypyrrole and Carbon X-Aerogel in Lithium–Oxygen Batteries

*Christine H.J. Kim[a], Chakrapani V. Varanasi[*b] and Jie Liu[*a]*

[a.] Department of Chemistry, Duke University, Durham, North Carolina 27708, United States. E-mail: j.liu@duke.edu

[b.] Army Research Office, Durham, North Carolina 27703, United States. E-mail: chakrapani.v.varanasi.civ@mail.mil

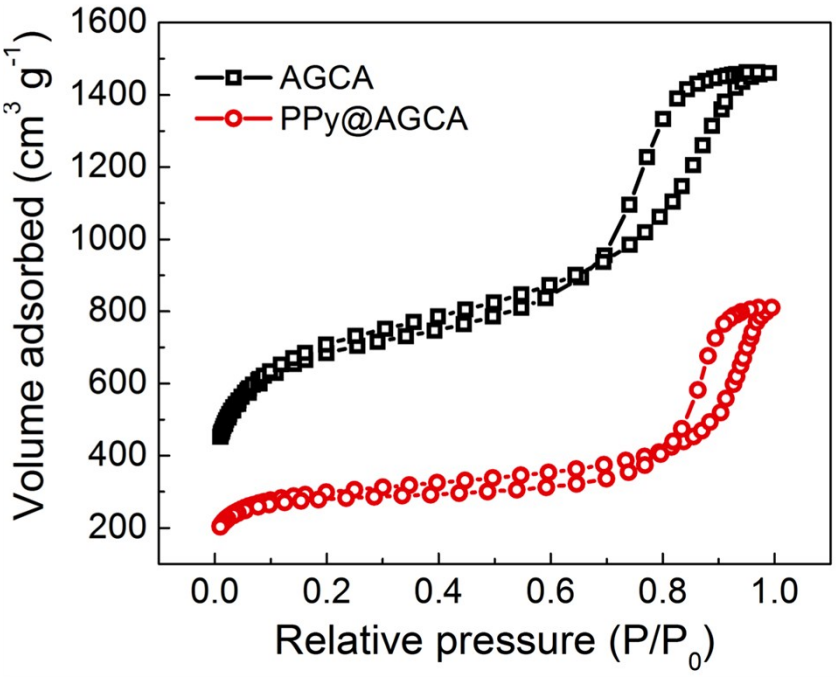

Figure S1. N_2 adsorption–desorption isotherms of AGCA and PPy@AGCA.

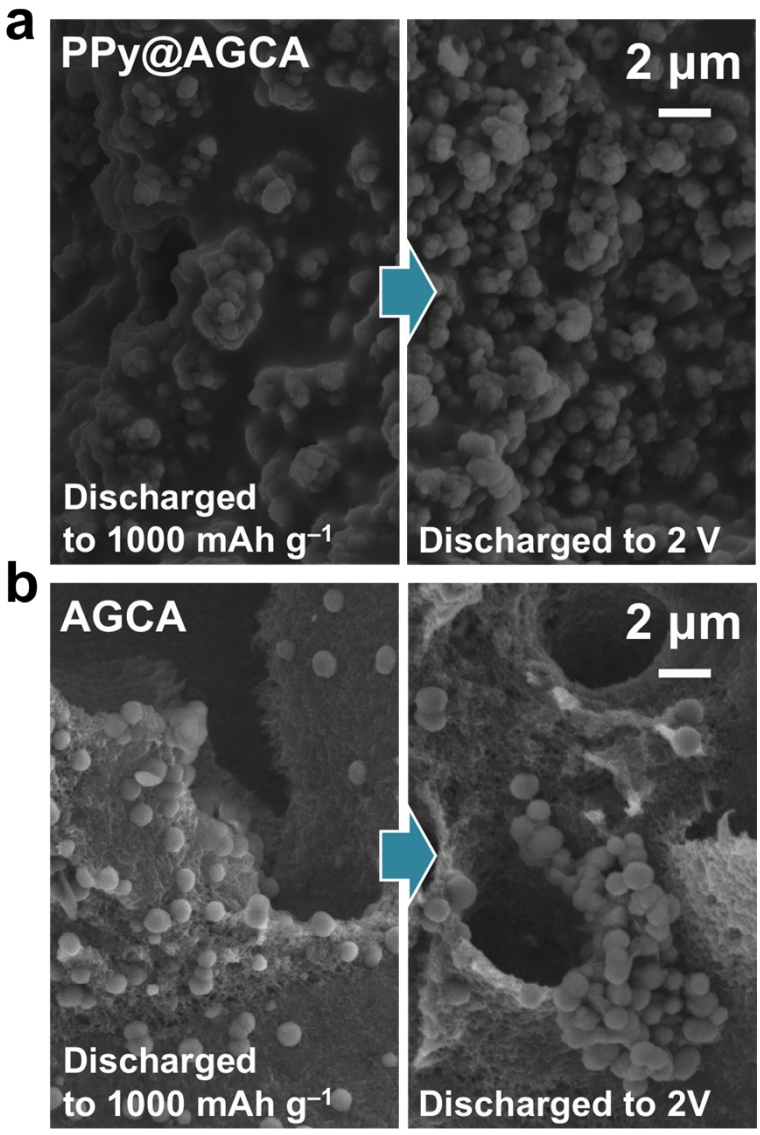

Figure S2. SEM images of (a) PPy@AGCA and (b) AGCA at different depths of discharge.

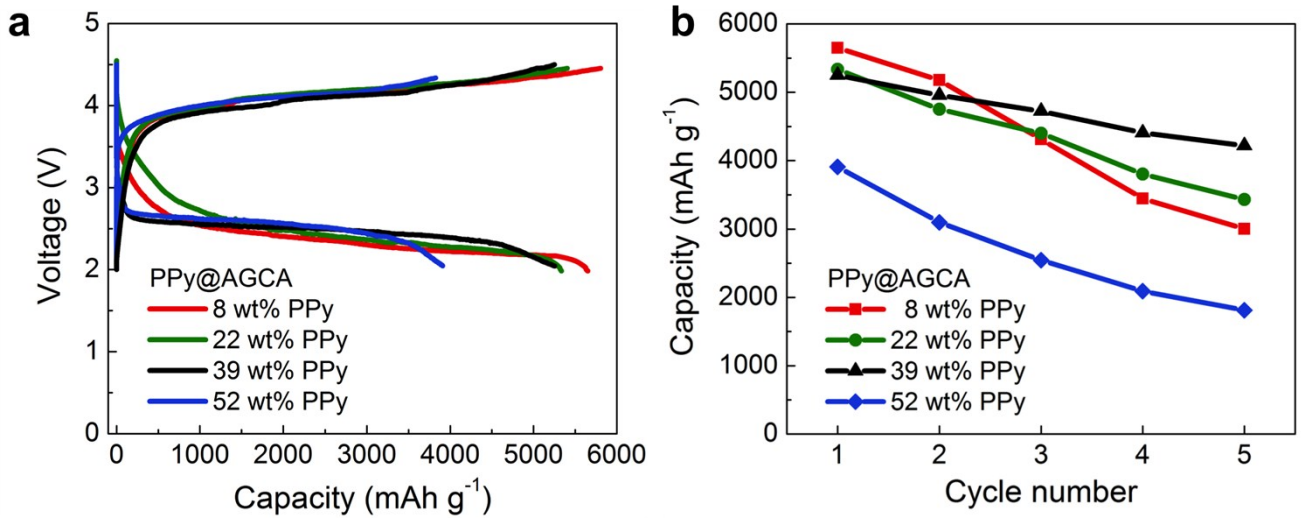

Figure S3. (a) Discharge–charge profiles of AGCA and PPy@AGCA with different PPy loadings (8, 22, 39, and 52 wt%) at a current density of 200 mA g^{-1}. (b) Calculated capacities (mAh g^{-1}) of PPy@AGCA with different PPy loadings against cycle number.

Note that further increase of PPy content to 52 wt% significantly lowers the capacity and the reversibility. This observation can be explained by the clogging of pores by an excessive amount of PPy, resulting in a decrease in electroactive surface area and further preventing oxygen diffusion into the inner region. Furthermore, such an undesired excessive PPy could increase ohmic resistance, thus leading to poor capacity retention upon cycling.[26,27]

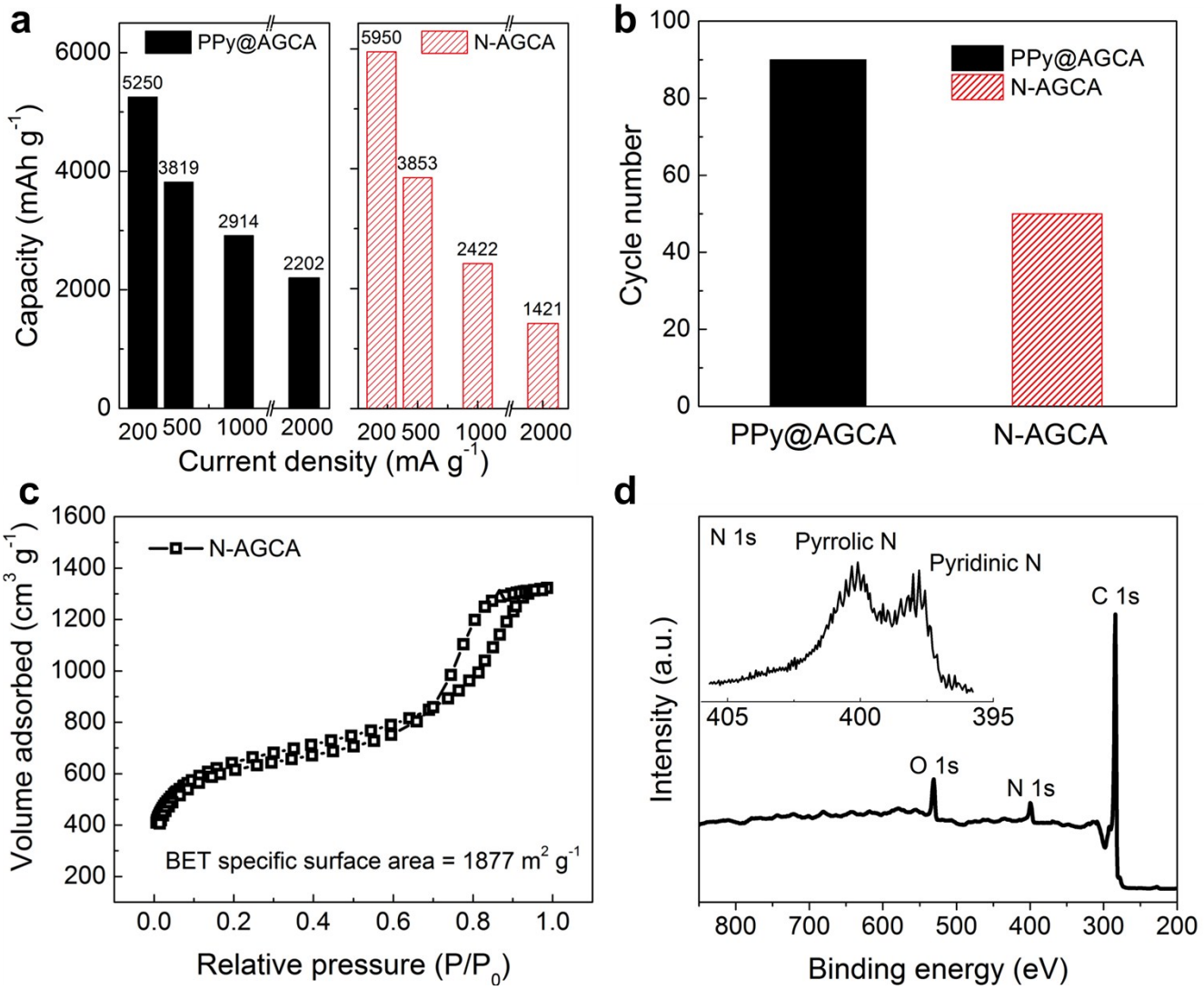

Figure S4. (a) Calculated capacities (mAh g^{-1}) of PPy@AGCA and N-AGCA at different current densities (200, 500, 1000, and 2000 mA g^{-1}). (b) Cycle number of PPy@AGCA and N-AGCA without capacity fading. (c) N_2 adsorption–desorption isotherms of N-AGCA. (d) XPS survey and high-resolution N 1s (inset) spectra.

The XPS analysis reveals the presence of C, N, and O elements in N-AGCA with a nitrogen content of 4.7 at%. The peaks observed in the high-resolution N 1s spectrum at 398.1 and 400.3 eV can be assigned to pyridinic and pyrrolic nitrogen, respectively.

Mechanical Properties

We performed compression tests, in which measurements of both hardness and elasticity were made. **Figure S5**a shows the stress–strain curves of AGCA, PPy@AGCA, and N-AGCA at 20% strain. We observed for AGCA, a transition from elastic to plastic behavior at 14.8% strain, where yielding occurs due to local buckling and collapse. For PPy@AGCA, however, no yielding is marked, which signifies that PPy strongly contributes to the material elasticity, thus making the aerogel matrix to be reversibly compressed in response to applied stress. More importantly, in comparison to N-AGCA, remarkable improvements in stiffness and strength are obtained for PPy@AGCA, in which the Young's modulus reaches 1.02 MPa, three folds greater than that of N@AGCA. Therefore, the cross-linked, hierarchical matrix of PPy@AGCA was proved to maximize the strength, stiffness and stability.

Such enhanced mechanical properties are further examined at higher strains (ε = 30%, 40%) in Figure S5b. It is confirmed that PPy coating increases the deformation resistance to the applied force, thus allowing PPy@AGCA to be compressed up to 40% and recovered by ≈75%. In addition, the mechanical stability of PPy@AGCA was further investigated by cyclic compression at 20% and 30% strains (Figure S5c,d). We found no noticeable degradation in stress and strength during the second and following cycles of compression. This stable behavior seems to be related to strong multipoint cross-linkage within the aerogel framework. As presented in Figure S5d,e, PPy@AGCA recovers its deformation with negligible mechanical failure, while retaining over 81% of maximum stress and recovering to ≈98% of original height even after the fifth cycle of compression at 30% strain. In contrast, we observed severe structural failure for N-AGCA, which began to break into multiple pieces at the first cycle, and thereafter completely collapsed after the fifth cycle (Figure S6). This, once again, illustrates the significance of coupling between PPy and AGCA, which provides the desired level of mechanical performance and eventually results in stable cycling performance.

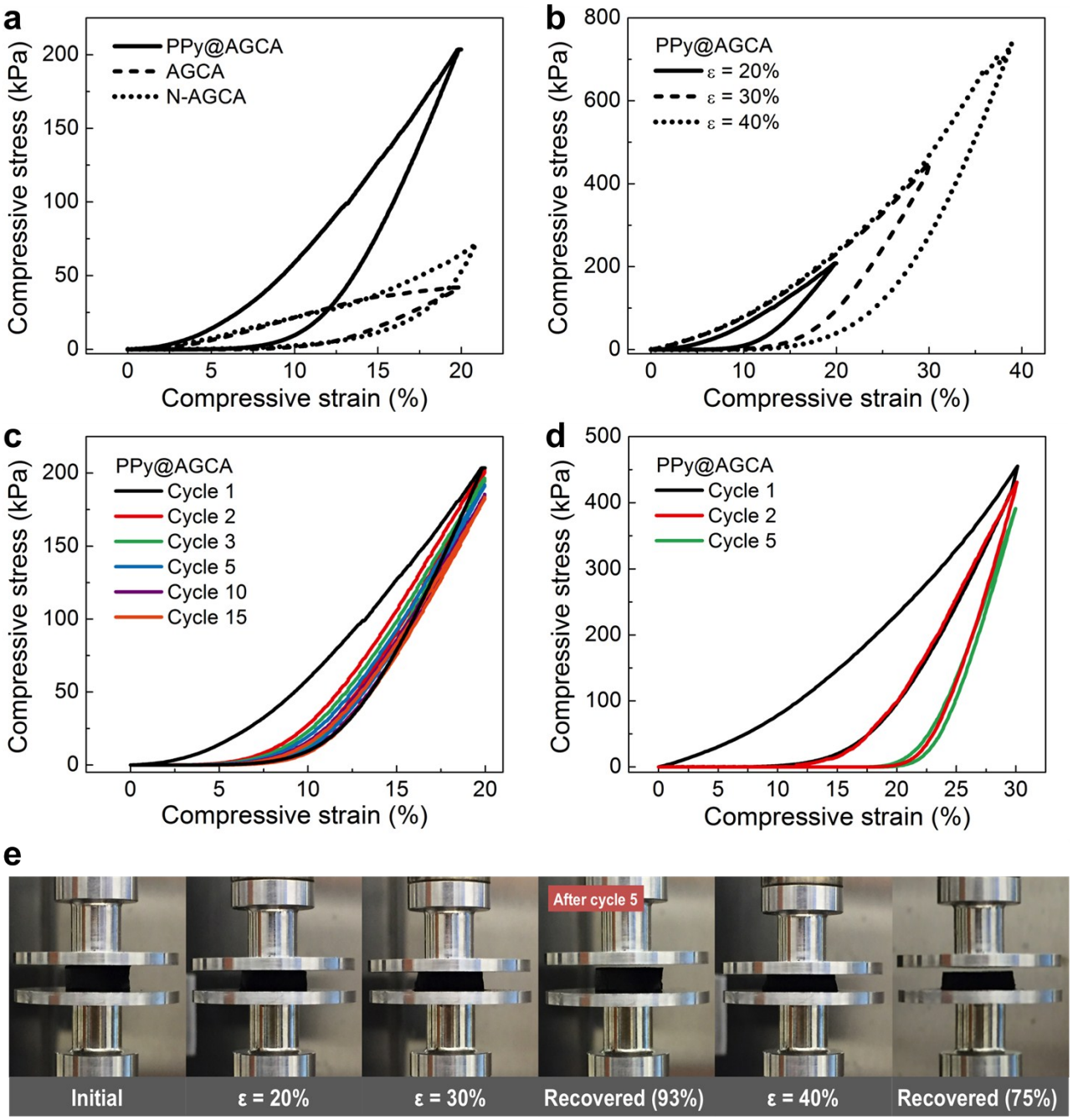

Figure S5. Compressive stress–strain curves of (a) PPy@AGCA, AGCA, and N-AGCA at a strain (ε) of 20 %, and (b) PPy@AGCA at different strains (ε = 20, 30, and 40%). (c, d) Cyclic stress–strain curves of PPy@AGCA at (c) ε = 20% and (d) 40%. (e) Optical images of PPy@AGCA after compression.

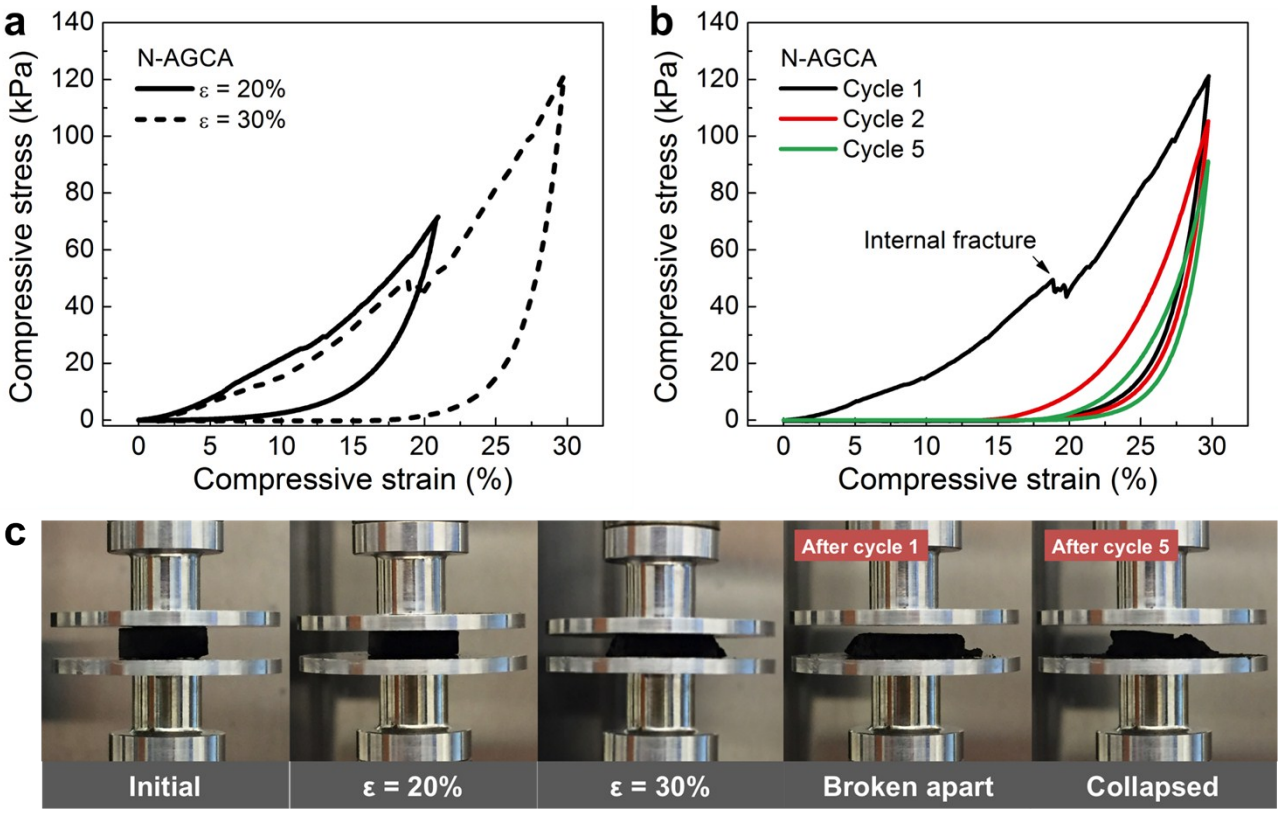

Figure S6. (a) Compressive stress–strain curves of N-AGCA at ε = 20% and 30%. (b) Cyclic stress–strain cures of N-AGCA at ε = 20%. (c) Optical images of N-AGCA after compression.

Table S1. Specific surface area, total pore volume, and micropore volume of AGCA and PPy@AGCA.

Sample	Specific surface area [$m^2\ g^{-1}$]	Total pore volume [$cm^3\ g^{-1}$]	Micropore volume [$cm^3\ g^{-1}$]	Mesoporosity [%]
AGCA	2244	2.34	0.82	65.0
PPy@AGCA (8 wt% PPy)	892	1.64	0.51	68.9
PPy@AGCA (22 wt% PPy)	801	1.40	0.43	69.2
PPy@AGCA (39 wt% PPy)	743	1.25	0.29	76.8

* Mesoporosity was calculated by dividing the mesopore volume by the total pore volume. Mesopore volume was estimated by subtracting the micropore volume from the total volume.

Table S2. Bulk density and conductivity of AGCA and PPy@AGCA.

Sample	**Bulk density [mg cm^{-3}]**	**Bulk conductivity [S cm^{-1}]**
AGCA	53.5	3.05
PPy@AGCA (8 wt% PPy)	58.2	1.62
PPy@AGCA (22 wt% PPy)	68.7	1.19
PPy@AGCA (39 wt% PPy)	87.7	0.98

Table S3. Comparison of performance of AGCA and PPy@AGCA with carbon-based oxygen electrodes reported in the literature.

Cathode	Density [mg cm^{-3}]	Overpotential [V]	Gravimetric capacity [mAh g^{-1} (at mA g^{-1})]	Volumetric capacity [mAh cm^{-3} (at mA g^{-1})]	Areal capacity [mAh cm^{-2} (at mA cm^{-2})]	Stability [Number]	Reference
PPy@AGCA	**87.7**	**1.38**	**5250 (200)** **2914 (1000)**	**460.4 (200)** **255.6 (1000)**	**32.2 (1.23)**	**90**	**This work**
AGCA	53.5	2	3500 (200) 1312 (1000)	187.2 (200) 70.2 (1000)	13.1 (0.75)	33	This work
Graphene-carbonized melamine foam	N/A	1.8	4100 (50) 1800 (200)	N/A	N/A	21	17
Graphene@g-C_3N_4	N/A	1.35	7100 (200) 2800 (300)	N/A	14.2 (0.4)	105	35
Ultrathin graphene sheet-assembled framework	4.2	1.45	21507 (200) 13271 (1000)	90.3 (200) 55.7 (1000)	17.9 (0.17) 3.8 (2.0)	42	36
Nitrogen and sulfur co-doped graphene nanosheet	N/A	1.38	11000 (200) 4100 (300)	N/A	N/A	38	37
N-doped nanoporous graphene	33.4	1.9	10400 (200)	346.8 (200)	2.4 (0.046)	100	38, 39
Ruthenium functionalized graphene aerogel	15.1	1.65	10000 (67)	150.8 (67)	15.2 (0.1)	30	40
Dry-pressed holey graphene	N/A	1.45	7667 (20) 2824 (100)	N/A	37.3 (0.1)	15	41
Macroporous interconnected hollow carbon nanofiber	12	1.3	11150 (1000) 7700 (2000)	133.8 (1000) 94.8 (2000)	N/A	110	42
Pd modified carbon nanotube (CNT) sponge	33.3	1.3	9092 (50) 4930 (200)	300 (50) 163 (200)	4.9 (0.2)	16	43

* Volumetric and areal capacities were estimated by multiplying the gravimetric capacity by the volumetric and areal densities given in the literature.